Int J Earth Sci (Geol Rundsch) (2016) 105:2241–2252
DOI 10.1007/s00531-015-1284-x

ORIGINAL PAPER

Sedimentary basin analysis using airborne gravity data: a case study from the Bohai Bay Basin, China

Wenyong Li[1] · Yanxu Liu[1] · Jianxin Zhou[1] · Xihua Zhou[1] · Bing Li[1]

Received: 26 March 2015 / Accepted: 3 December 2015 / Published online: 15 December 2015

Abstract In this paper, we discuss the application of an airborne gravity survey to sedimentary basin analysis. Using high-precision airborne gravity data constrained by drilling and seismic data from the Bohai Bay Basin in eastern China, we interpreted faults, structural elements, sedimentary thickness, structural styles and local structures (belts) in the central area of the Basin by the wavelet transform method. Subsequently, these data were subtracted from the Bouguer gravity to calculate the residual gravity anomalies. On this basis, the faults were interpreted mainly by linear zones of high gravity gradients and contour distortion, while the sedimentary thicknesses were computed by the Euler deconvolution. The structural styles were identified by the combination of gravity anomalies and the local structures interpreted by the first vertical derivative of the residual gravity. The results showed evidence for seven faults, one sag and ten new local structure belts.

Keywords Airborne gravity · Sedimentary basin · Anomaly separation · Gravity inversion · Bohai Bay Basin

Introduction

Sedimentary basins are often analyzed with seismic and drilling data. However, airborne gravimetry of sedimentary basins in complex geographic regions, such as onshore–offshore transition zones, has made important progress in large to mid-scale geological–geophysical and mineral resource surveys in some developed countries with gravity anomaly accuracy up to 1–2 mGal and half-wavelength resolution up to 1 km (Diehl et al. 2008; Dransfield and Zeng 2009; Forsberg and Olesen 2010; Schwabe et al. 2012; Kass 2013; Keating and Pilkington 2013; McAdoo et al. 2013; Forsberg et al. 2014; Pacino et al. 2014). Although there have been many studies on airborne gravity surveys, it was seldom reported that sedimentary basins were systematically investigated using airborne gravity data.

The adoption of additional geophysical methods is important and meaningful for geological surveys and mineral resource exploration of sedimentary basins in complex geographic regions such as onshore–offshore transition zones. To increase activity in exploration areas of complicated geographic regions, China introduced an advanced airborne gravity survey system (GT-1A) and conducted a series of tests and surveys over the past few years (Li et al. 2010a, b, 2013, 2014). Based on the acquired airborne gravity data over the southwestern Bohai Sea and onshore–offshore transitional zone, this study investigates the central area of the Bohai Bay Basin and discusses the faults, structural elements and styles, sedimentary thickness and local structures.

Geological setting

The study area is located in the central part of the Bohai Bay Basin in the North China Craton (Fig. 1). This area belongs to the North China Plain subprovince of the North China stratigraphic province (Su et al. 2011; Li et al. 2012). The pre-Cenozoic strata are concealed, and the entire region is covered by either Quaternary sediments or seawater. Previous seismic and drilling exploration has exposed the buried strata in the study area and discovered some oilfields (Zhou et al. 2003). According to the drilling data, the late Ordovician to

✉ Wenyong Li
liwy66@163.com

[1] China Aero Geophysical Survey and Remote Sensing Center for Land and Resources, Beijing 100083, China

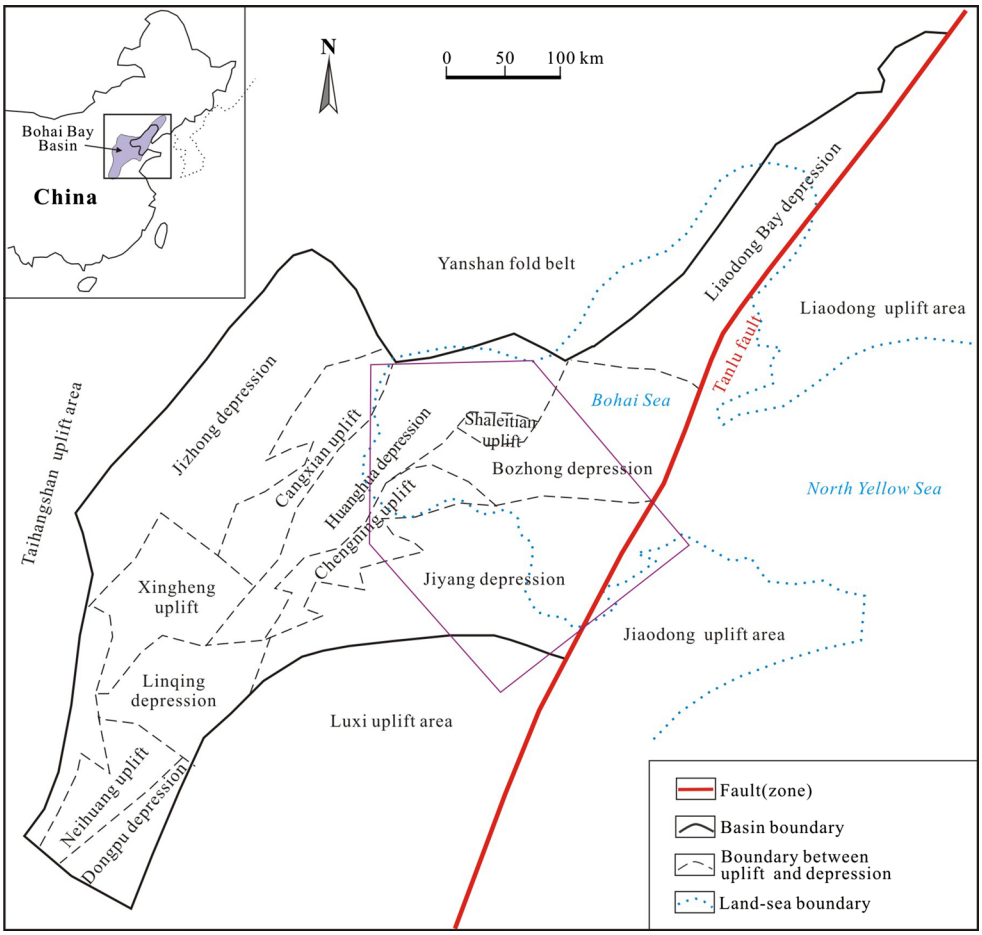

Fig. 1 Sketch tectonic map showing the location of the study area (modified after Zhou et al. 2003). The purple polygon is the area covered by the airborne gravity data, which corresponds to the area of Figs. 2, 3, 4, 7, 9 and 13

early Carboniferous and Triassic are absent, and the stratigraphic column includes (Table 1) Archean–Paleoproterozoic (metamorphic facies), Meso-Neoproterozoic (marine carbonate facies), Cambrian–middle Ordovician (platform marine carbonate facies), late Carboniferous–Permian (marine-terrigenous facies), Jurassic–Cretaceous (continental and volcanic facies) and Cenozoic (continental facies). Within the latter strata, the terrestrial Paleogene is about 5000 m thick, with abundant oil and gas resources; thus, it is the main exploration target. The NNE-trending Tanlu fault crosses the eastern part of the study area and constitutes the eastern boundary of the Bohai Bay Basin. The Tanlu fault controlled the sedimentary thickness, structural framework and pattern of the Bohai Bay Basin during the Meso-Cenozoic.

Data

The airborne gravity survey over the study area was carried out using the Russian GT–1A airborne gravimeter system, covering an area of 50,120 km^2. The spacing of adjacent survey lines was 1 km, with a survey line direction of 140°–320°, and a cross line spacing of 10 km with a direction of 90°–270°. The flight altitude was 450 m above sea level. The internal and external overall conformity accuracy of the repeated lines' root-mean-square is 0.4 and 1.1 mGal (1 mGal = 10^{-5} m/s^2), respectively, and the total accuracy of free-air gravity anomalies after leveling and noise processing is 0.5 mGal.

The airborne gravity data processing included two phases: field preprocessing and indoor processing. The field preprocessing included differential global positioning system (DGPS) data solution, assessment of quality control, computation of free-air gravity, workload statistics, flight level and yawing distance. The DGPS data solution refers to the combination of data recorded by DGPS and gravimeter inertial navigation system (INS) platform, solution of coordinates, velocities and accelerations of the INS platform. The free-air gravity anomalies were calculated as follows. First, we carried out graphic display and time selection of the data from the gravity sensor positioning, INS platform attitude, velocity of DGPS calculation, preflight reference and post-flight reference of gravity base station and primary gravity measurement. Then, we made corrections to the primary gravity data, including vertical and horizontal acceleration corrections, attitude correction, Eotvos correction, drift adjustment and base correction, normal gravity field correction and altitude correction (reduction to sea level). Finally, we obtained airborne free-air

Table 1 Stratigraphy in Bohai Bay Basin (modified after Zhou et al. 2003)

Strata		Age (Ma)	Tectonic movement	Major lithology	Thickness (m)
Cenozoic	Quaternary	2.6	Himalayan movement	Clay layer and sand layer	253–660
	Neogene	23		Sandy conglomerate, sandstone and mudstone	833–3314
	Paleogene	66		Mudstone, sandstone, sandy conglomerate, with oil shale and bioclastic limestone interbeds	230–5377
Mesozoic	Cretaceous	146	Yanshanian movement	Sandstone, siltstone, mudstone, andesite, tuff	26–736
	Jurassic	252		Sandy conglomerate, sandstone, mudstone, coal, andesite, basalt, tuff	13–587
Paleozoic	Permian Carboniferous	416	Variscan movement	Sandstone, siltstone, mudstone, limestone, coal	93–824
	Ordovician Cambrian	541	Caledonian movement	Limestone	188–1478
Meso-Neoproterozoic		1800	Jinning movement	Dolostone, limestone, sandstone, siltstone, shale	>1200
Archean–Paleoproterozoic			Luliang movement	Amphibolite, gneiss, schist, phyllite, granulitite, migmatite	>3000

gravity anomaly data for the survey line using the fast Fourier transform (FFT) low–pass filter (100-s wavelength window). The indoor processing involved coordinate transformation, data editing and leveling, noise processing, quality assessment, basic graphics drawing, airborne Bouguer gravity calculation (terrain and stone-slab correction) and potential field transformation (including first and second vertical derivative, upward continuation, directional derivative, residual anomaly of Bouguer gravity). Among these, the airborne Bouguer gravity calculation was especially important. We calculated the airborne Bouguer gravity anomalies in the study area using the terrain correction and stone-slab correction modules in the Oasis Montaj software (Geosoft Inc., Canada). The chosen parameters included an average rock density of 2.67 g/cm^3, seawater density of 1.03 g/cm^3 and terrain correction radius of 166.7 km. After data processing and correction, we obtained an airborne Bouguer gravity data grid of 500 × 500 m.

Methods and results

Geophysical basis

The heterogeneous distribution and density contrasts of rocks or strata are the cause of gravity anomalies (Ball et al. 2013; Choi et al. 2013). Therefore, the densities of rocks or strata are the basis for modeling and interpretation of airborne gravity anomalies. The undulation and sudden change characteristic of a density interface reflect geological or tectonic features, such as faults, magmatic rocks, uplift or swell, depression or sag, and often cause gravity anomalies, such as zones of high gravity gradients, gravity contour distortion and gravity highs or lows. Thus, the faults, magmatic rocks and structural elements can be interpreted and inversed by characterizing gravity anomalies.

By analyzing the density data from exploration work in our study area, we distinguished two main density layers in the sedimentary strata, namely a Cenozoic layer (average density of 2.19 g/cm^3) and a pre-Cenozoic layer (average density of 2.68 g/cm^3). There is a clear density interface between the two layers with a contrast of 0.49 g/cm^3. This distinct density interface with lateral changes or dipping provides favorable geophysical prerequisites for the separation of airborne gravity anomalies.

Gravity anomaly separation

Gravity anomalies are responses to the gravitational effect of multiple heterogeneous geological bodies with different scales, patterns and depths (Lucke 2014; Oruc 2014). The

Cenozoic sediments and the basement relief are the subjects of the present airborne gravity survey, so to extract the gravity anomalies caused by them from the observed Bouguer gravity anomalies is the key to this work. Through a comparison of anomaly separation methods, we used wavelet transform to decompose the gravity anomaly and achieve a better result.

The wavelet transform is a timescale domain technology. It can decompose the real signal into different scales and thus resolve the instantaneous parameters of the real signal for each scale (Fedi and Cascone 2011; Beiki 2013; Gutierrez et al. 2013; Kunagu et al. 2013; Martin et al. 2013; Goyal and Tiwari 2014; Aguilar-Rodriguez et al. 2014; Harlan 2014; Yuan and Simons 2014).

The continuous wavelet transform (CWT) is defined as:

$$(\mathrm{CWT}_{\psi} f)(a,\tau) = |a|^{-\frac{1}{2}} \int_{-\infty}^{+\infty} f(t)\overline{\psi\left(\frac{t-\tau}{a}\right)}\mathrm{d}t \tag{1}$$

where a and τ are the scale and the translation parameter, respectively, and $\psi_{(a,\tau)}(t)$ is the wavelet function (simply called wavelet), which is defined as:

$$\psi_{(a,\tau)}(t) = |a|^{-\frac{1}{2}}\psi\left(\frac{t-\tau}{a}\right), \quad a \in R, a \neq 0; \tau \in R \tag{2}$$

where R is the real number domain, and $|a|^{-\frac{1}{2}}$ is the normalization factor.

By substituting Eq. (2) into Eq. (1), the expression of $(\mathrm{CWT}_{\psi} f)(a,\tau)$ can be easily written as:

$$(CWT_{\psi} f)(a,\tau) = \int_{-\infty}^{+\infty} f(t)\overline{\psi_{a,\tau}(t)}dt = \langle f, \psi_{a,\tau} \rangle \tag{3}$$

Based on Eq. (3), the inverse transform equation for a continuous wavelet can be written as:

$$f(t) = C_{\psi}^{-1} \int_{-\infty}^{+\infty} \int_{-\infty}^{+\infty} (\mathrm{CWT}_{\psi} f)(a,\tau)\psi_{a,\tau}(t)\frac{\mathrm{d}a}{a^2}\mathrm{d}\tau \tag{4}$$

We introduced $a = a_0^j$ and $\tau = ka_0^j\tau_0$ into Eq. (2), and the discrete wavelet ($\psi_{j,k}$) can then be expressed as:

$$\psi_{j,k}(t) = a_0^{-\frac{j}{2}}\psi\left(\frac{t - ka_0^j\tau_0}{a_0^j}\right) = a_0^{-\frac{j}{2}}\psi(a_0^{-j}t - k\tau_0) \tag{5}$$

where a_0 and τ_0 are the discrete interval and the scale radix, respectively, and j and k are the nonnegative integer and integer, respectively.

The transform coefficient for the discrete wavelet can be expressed as:

$$C_{j,k} = \int_{-\infty}^{+\infty} f(t)\overline{\psi_{j,k}(t)}\mathrm{d}t = \langle f, \psi_{j,k} \rangle \tag{6}$$

The inverse transform equation derived from Eq. (6) can be written as:

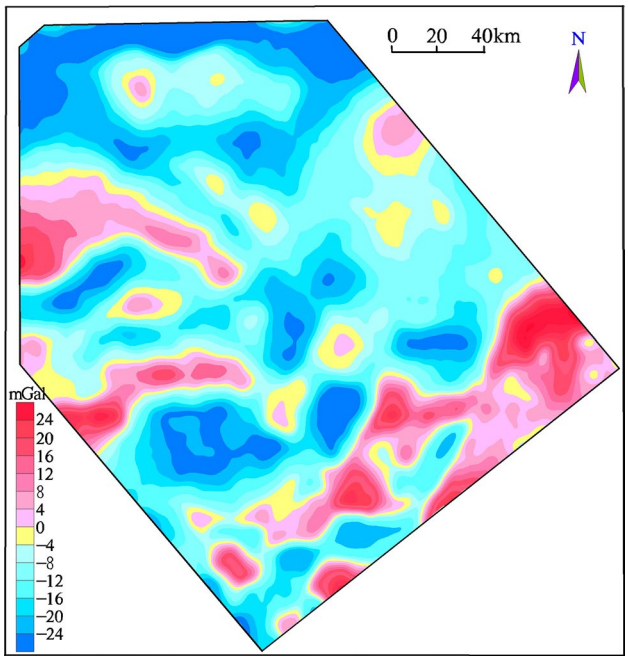

Fig. 2 Map of airborne Bouguer gravity anomalies in the survey area from airborne gravity data

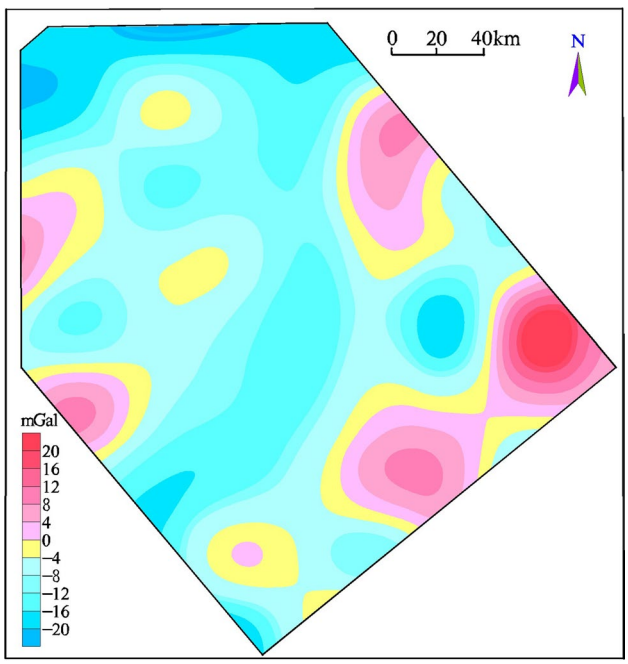

Fig. 3 The fourth-order wavelet approximation of Bouguer gravity

$$f(t) = C\sum_{-\infty}^{+\infty}\sum_{-\infty}^{+\infty} C_{j,k}\psi_{j,k}(t) \tag{7}$$

where C is a constant unrelated to the signal.

We assigned $\{V_j\}$ as the given multi-scale analysis. The multi-scale decomposition can then be expressed as

$$x_0 = x_1 + d_1 = x_2 + d_2 + d_1 = \cdots = x_N + d_N + d_{N-1} + \cdots + d_2 + d_1 \quad (8)$$

Essentially,

$$x \approx x_N + \sum_{i=1}^{N} d_i \quad (9)$$

where $x_i \in V_j$ represents an approximation of the function $x \in L^2(R)$ with the resolution of 2^{-j}(low-frequency components of the function x), and $d_i \in W_j$ represents the approximation error, namely the high-frequency components of the function x.

By 2D wavelet transform, the grid data can be decomposed into the low-frequency and the high-frequency coefficients in the horizontal, vertical and diagonal directions. For example, the gravity anomaly $G(x, y)$ can be decomposed as:

$$G(x,y) = a_N g(x,y) + \sum_{j=1}^{N} (dh_j g(x,y) + dv_j g(x,y) + dd_j g(x,y)) \quad (10)$$

where for $G(x, y) \in \{V_j^2\}$, j is the positive integer, $a_N g(x, y)$ is the approximation of the low-frequency components for the N-order wavelet transform, and $dh_j g(x, y)$, $dv_j g(x, y)$ and $dd_j g(x, y)$ are the high-frequency components in the horizontal, vertical and diagonal directions for the j-order wavelet transform.

The map of airborne Bouguer gravity anomalies of the study area shows the comprehensive response to all the underground heterogeneous geological bodies (Fig. 2). By calculating the source's average depth to the fourth-order wavelet approximation, the anomaly is 7.8 km (Fig. 3). According to the seismic and drilling data, the maximum depth to the Cenozoic basement is about 9.2 km (Zhou et al. 2003). Therefore, we define the fourth-order wavelet approximation as the gravity anomalies caused by the pre-Cenozoic Basin's basement density heterogeneity. To study the Cenozoic sedimentary basin, its thickness and structure, we subtracted the fourth-order wavelet approximation anomalies from the Bouguer gravity to determine the residual gravity anomalies (Fig. 4). The residual gravity anomalies are caused by the interface undulation between the Cenozoic and the pre-Cenozoic strata and Cenozoic density heterogeneities. These anomalies form the basis for our subsequent interpretations.

The differences are shown clearly in the local Bouguer gravity high in the northeast of the study area (Fig. 2) decomposed into the local residual gravity low (Fig. 4) and the fourth-order wavelet approximation gravity high (Fig. 3). According to the seismic and drilling data (Zhou et al. 2003), the local residual gravity low corresponds to the deep concave belt in the Bozhong sag; thus, the residual gravity shown in Fig. 4 is consistent with the Cenozoic features and can be used to interpret the Cenozoic strata.

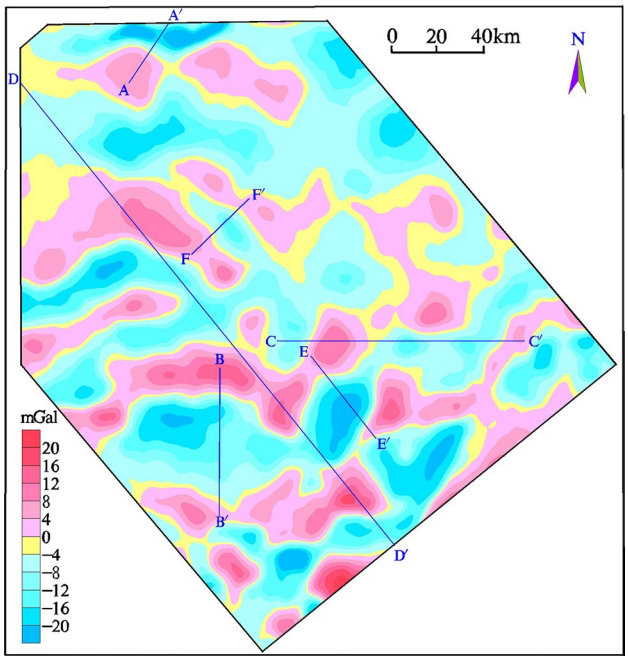

Fig. 4 Residual gravity anomalies map of the survey area. The residual gravity anomalies were obtained by removing the fourth-order wavelet approximation anomalies (caused by the basin basement (pre-Cenozoic) density inhomogeneities) from the Bouguer gravity. *A* and *A′*, *B* and *B′*, *C* and *C′*, *D* and *D′*, *E* and *E′*, *F* and *F′* are the locations of the sections shown in Figs. 6, 8, 11 and 12

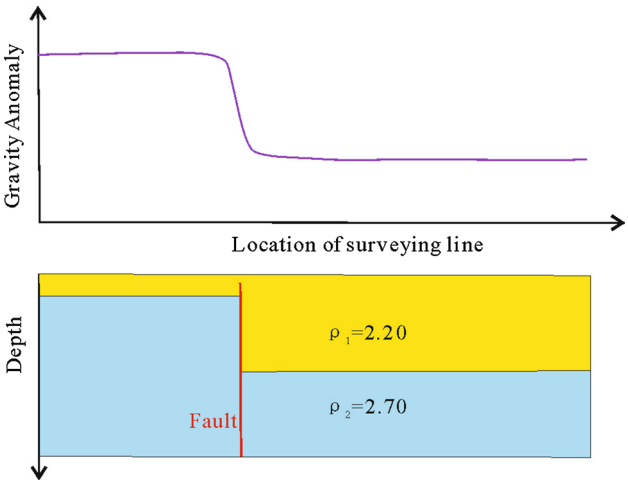

Fig. 5 Theoretical model of a vertical fault and its gravity response

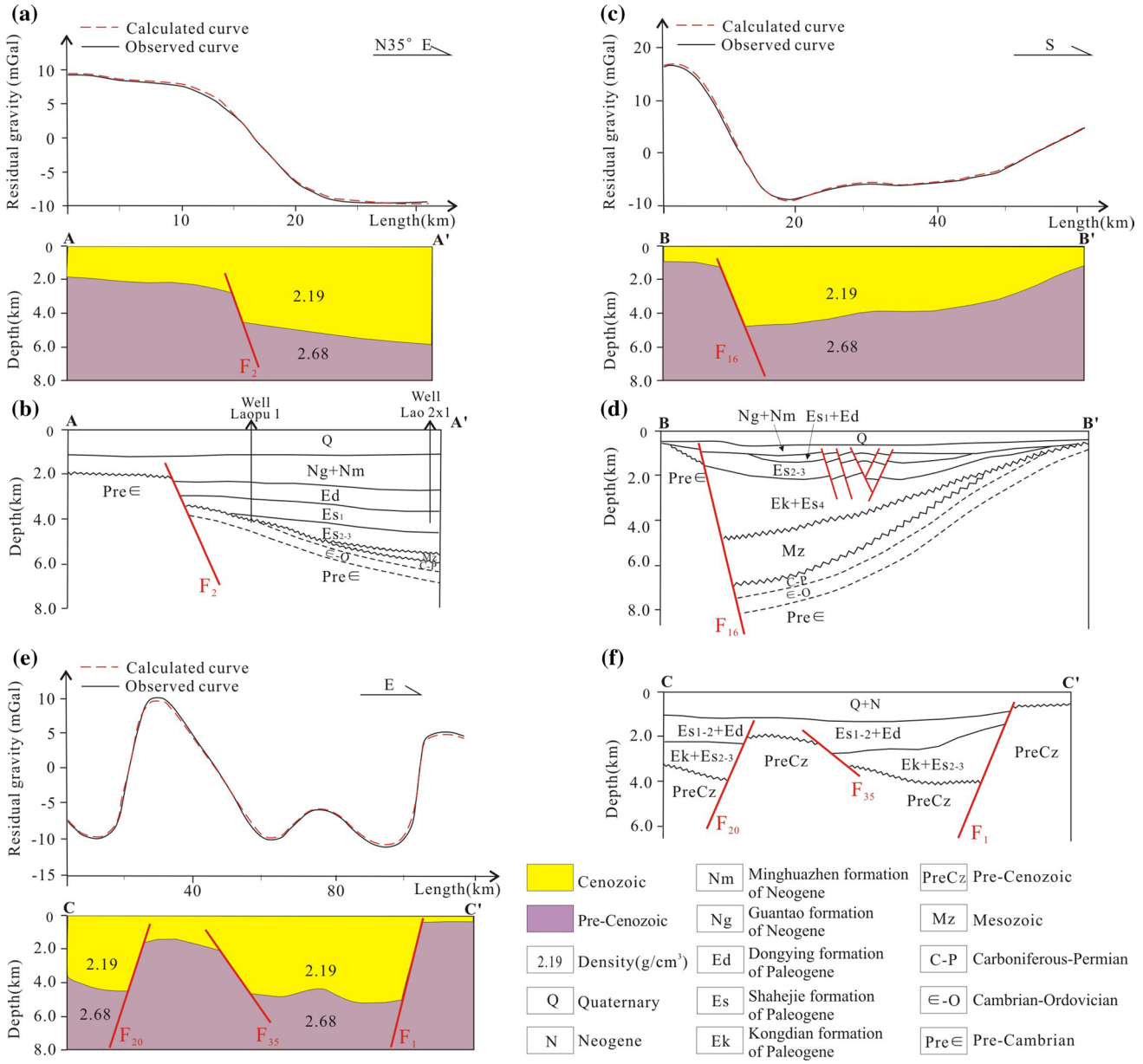

Fig. 6 2D density sections derived from gravity forward inversion (**a**, **c**, **e**) and corresponding seismic–geological sections (**b**, **d**, **f**, modified after Zhou et al. 2003). The locations of the sections are shown in Fig. 4

Fault interpretation

A fault causes the displacement and dislocation of strata and results in density differences and thus also of gravity anomalies. Figure 5 shows the theoretical model of a vertical fault and its gravity response, which shows that there is an obvious high gravity gradient corresponding to the fault. Figure 6 displays the comparison between 2D gravity inversion sections (Fig. 6a, c, e) and the seismic–geological sections (Fig. 6b, d, f) in the survey area, demonstrating that the faults, F_2, F_{16}, F_{20}, F_{35} and F_1 inversed by gravity anomalies, are basically consistent with the seismic and drilling data. The faults F_2, F_{16}, F_{20}, F_{35} and F_1 all correspond to high gravity gradients. If a fault is strike–slip, it will cause a gravity anomaly displacement along the strike. So, we can interpret faults by gravity anomaly inversions, and the interpretations are reliable. For 2D gravity inversions, the density parameters were consistent with the measured data, and the depths to the density interface were constrained by known seismic and drilling data. If there are no suitable density and depth parameters as constraints, the multiplicity of gravity inversion is increased, resulting in indeterminate or erroneous consequences.

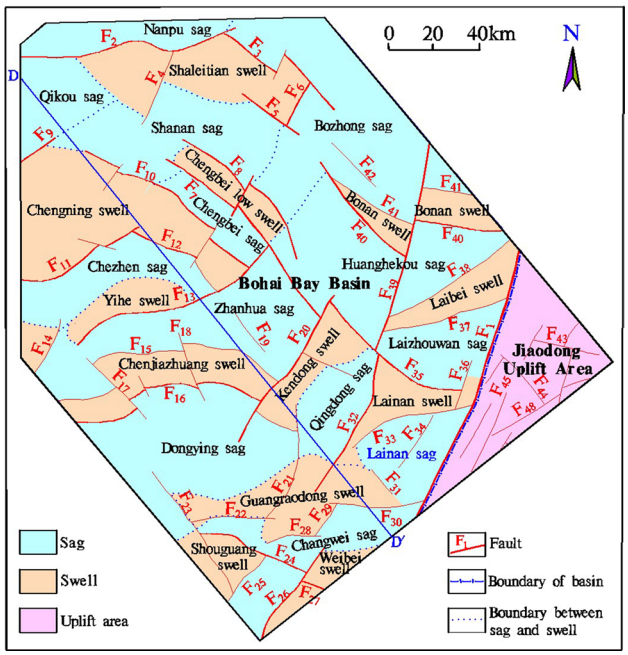

Fig. 7 Fault system and structural elements in the survey area. D and D′ is the location of the section shown in Fig. 8

Based on the residual gravity (Fig. 4) and the Bouguer gravity (Fig. 2), we interpreted the faults by the following signatures: (1) The division line between different gravity fields. There are usually different sediments with different densities on either of large-scale faults, which indicates that the gravity anomalies differ. Thus, a division line between different gravity anomalies usually suggests a large-scale fault. (2) Linear zone of high gravity gradient. A large- or medium-scale fault usually has two translocated sides that have different sediments and leads to the large density contrast between two sides of a fault. The fault usually causes a linear zone of a high gravity gradient, where the position of the fault is consistent with this zone. Therefore, linear zones of high gravity gradients are usually important markers for identifying faults. (3) Gravity contour distortion. Essentially, this is where the Bouguer gravity linear zone is dislocated or changes suddenly, indicating the earlier fault has been dislocated by the later fault. (4) Linear extreme belt or beaded extreme belt of the total gravity gradient amplitude. The total gravity gradient amplitude is similar to the directional derivative. The difference is that the total gravity gradient amplitude considers the total modulus of the Bouguer gravity gradient and the values of the modulus are always positive, whereas the gravity directional derivative gives the gradient of the Bouguer gravity along a given direction, and the positive or negative values depend on the direction. (5) Connection line along the edge of blocky gravity anomalies in a certain trend direction. The fault usually cuts and controls the distribution of geological blocks, so we can determine the fault according to the edges of subsequent blocky gravity anomalies reflecting different geological blocks. However, these signatures do not only apply to fault structures. For example, local density bodies, such as magmatic rocks, can also cause gravity contour distortions. However, according to the regional geological setting, the survey area is a Cenozoic faulted basin with many faults and fewer magmatic rocks. Thus, we strongly consider the above signatures for the interpretation of faults.

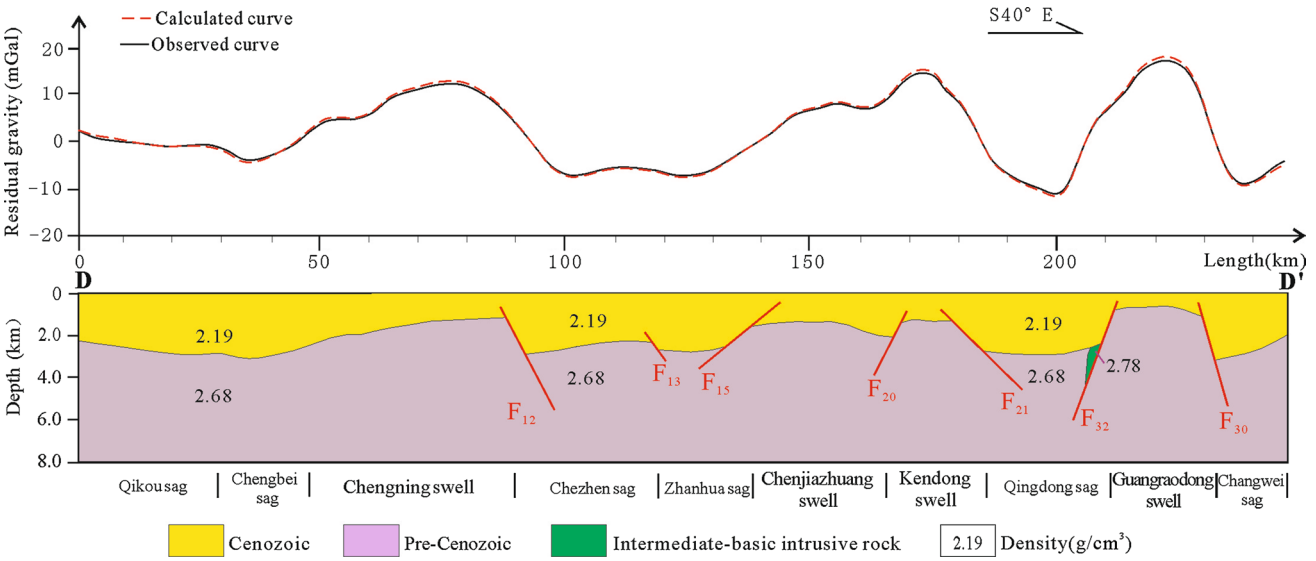

Fig. 8 2D density section derived from gravity forward inversion showing the faults and structural elements. The location of this section is shown in Figs. 4 and 7

Table 2 Structure index of different gravity anomaly sources

Gravity anomaly source	Structure index
Horizontal cylinder	1
Incline sheet and step	1
Sphere	2

We interpreted nearly 40 faults and then further divided the structural elements (Figs. 7, 8). Among them, seven faults and one sag are newly discovered by the present airborne gravity data. The faults are identified as F_{21}, F_{31}, F_{33}, F_{34}, F_{36}, F_{45} and F_{46} and the sag is named Lainan sag (at the south of the study area, marked in blue in Fig. 7). The majority of them are in the onshore–offshore transitional area.

Calculation of depth to Cenozoic basement

The Cenozoic basement is the main density interface in the study area, providing an advantageous geophysical precondition for gravity forward and inversion techniques. Based on the comparison of different potential field forward methods and inversion interpretation, we used the Euler deconvolution method (Fedi 2007; Salem 2011; Tedla et al. 2011; Fedi and Florio 2013; Lee et al. 2013; Khalil et al. 2014; Speranza and Minelli 2014; Vandas and Romashets 2014). We applied this method to the residual gravity data (Fig. 4) to calculate the depth to the Cenozoic basement in the study area. The structure index of different gravity anomaly sources is listed in Table 2. In the actual calculations, using known seismic and drilling data as constraints, we adjusted the parameters until the results conformed to the known data. No prior data were bound to the calculations to indicate that the errors were large or even that the results were wrong.

The Cenozoic basement shows the large variations of depth values between the swells and the sags (Fig. 9) using the Euler deconvolution method. The depth values in sags range from 3.0 to 7.5 km and the depth values in swells from 1.0 to 3.0 km. The maximum depth is located in the Bozhong sag (7.5 km), and the minimum depth (0.5 km) is located in the Jiaodong uplift area (on the east side of fault F_1), followed by Chengning, Chenjiazhuang and Lainan swells (1.0 km).

Identification of structural styles

The structural style refers to the sum of structures formed under a specific stress field. A specific structural style usually causes a specific gravity anomaly combination. Conversely, a specific gravity anomaly combination often reflects a specific structural style. This is the geophysical basis to study structural styles by gravity anomalies. According to the gravity anomaly combinations and their reflecting structural properties, we identify two kinds of structural styles.

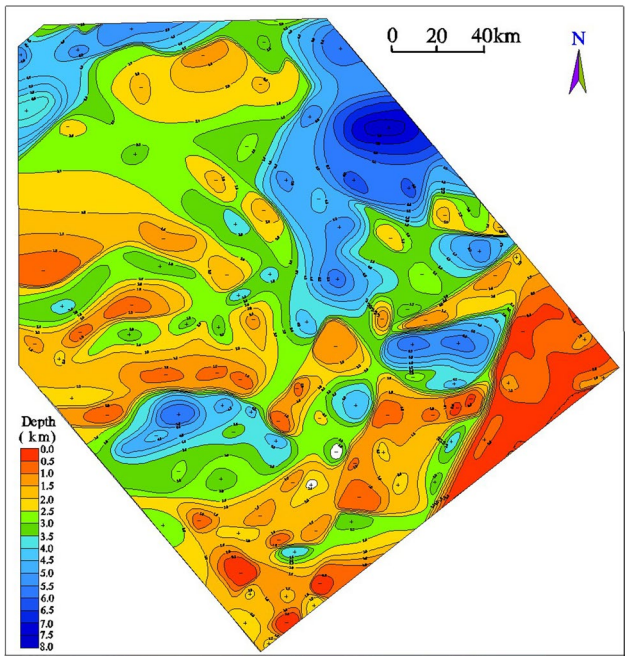

Fig. 9 Depth to the Cenozoic basement in the survey area

Extensional structural style

Extensional structural styles are the most common in the study area, represented mainly by normal faults and their combination caused by the extensional tectonic stress field. The two main styles are the single-fault-controlling sag and the double-fault-controlling sag. Figure 10 shows the theoretical models of the single-fault-controlling sag and its gravity response (Fig. 10a), and the double-fault-controlling sag and its gravity response (Fig. 10b). The single-fault-controlling sag results from the combination of a gentle gravity low on one side and a high gravity gradient on the other side, whereas the double-fault-controlling sag is the combination of a gravity low in the middle and two high gravity gradients on either side.

The single-fault style is characterized by the plane and the section showing the gravity anomalies combination of a linear zone of high gravity gradient on one side and a gentle gravity low on the other side. The amplitudes of the gentle gravity low gradually decrease with distance to the linear zone. The section shows the dustpan-like sag, with the main fault on one side and no obvious fault on the other side. An example of a single-fault style is the Dongying sag (Fig. 11).

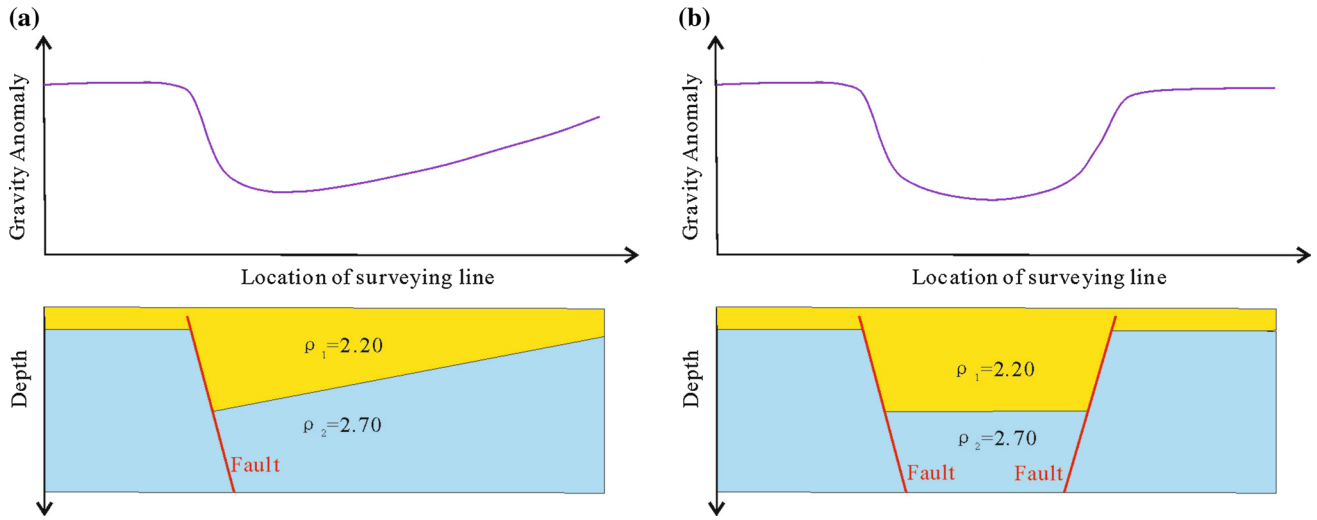

Fig. 10 Theoretical models of structural styles and their gravity responses. **a** A single-fault structural style and its gravity response; **b** A double-fault structural style and its gravity response

Fig. 11 The single-fault structural style (Dongying sag). **a** Residual gravity anomalies map; **b** forward and inverse section. The location of this map is shown in Fig. 4

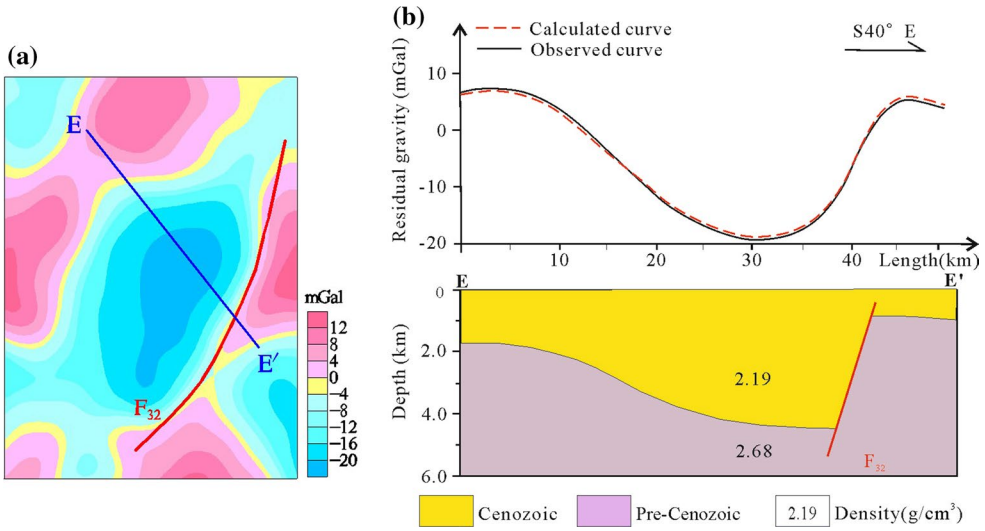

Fig. 12 The double-fault structural style (Chengbei sag). **a** Map of the residual gravity; **b** forward and inverse section. The location of this map is shown in Fig. 4

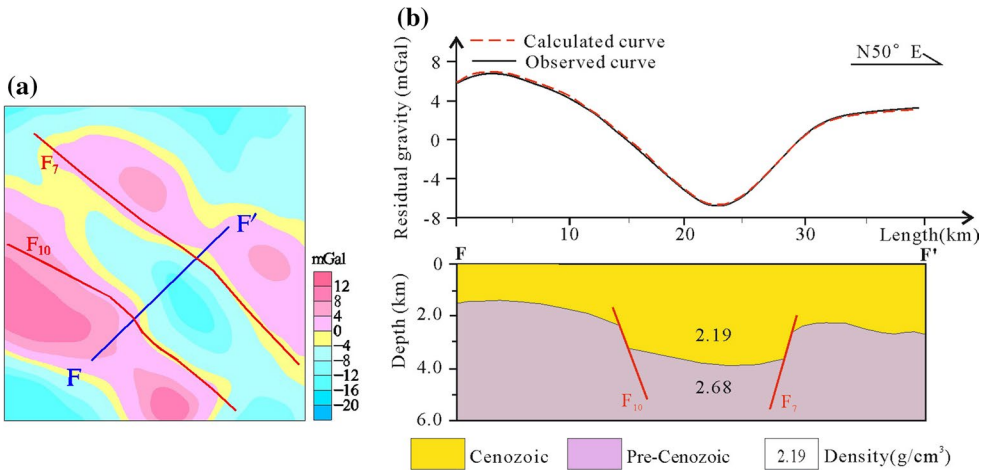

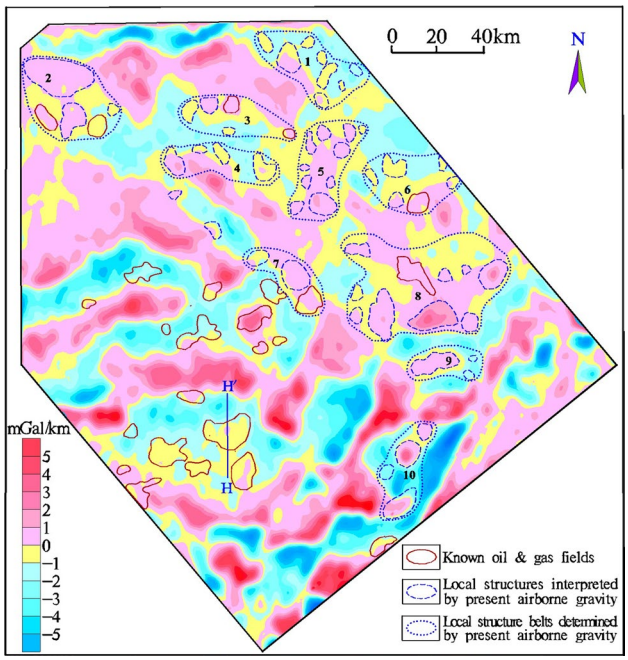

Fig. 13 Map of the first vertical derivative of the residual gravity in the survey area. The residual gravity refers to Fig. 4. H and H′ is the location of the seismic profile shown detail in Fig. 14

The double-fault style, represented by the Chengbei sag (Fig. 12), is characterized by the plane and the section showing the gravity anomaly combination of two linear zones of high gravity gradients on both sides and a gravity low in the middle. The section shows the faulted sag, developing inclination-to-inclination normal faults on both sides and thick sediments between the two faults.

Wrench structural style

Wrench structures and strike–slip faults are the important expressions of horizontal crustal movement. The main features of the wrench structural styles in the study area are mainly en-echelon faults, such as a series of faults running diagonal and parallel with a similar angle to the main fault. The faults F_{30}, F_{33}, F_{37}, F_{38} and F_{40}, located on the western side of fault F_1 in the eastern part of the study area, are NE–NEE trending and distributed in an en-echelon arrangement (Fig. 7). The linear zones of gravity gradient or the zones of gravity contour distortion reflect the faults F_{30}, F_{33}, F_{37}, F_{38} and F_{40} are also NE–NEE trending and distributed in an en-echelon arrangement; they also intersect the linear zone of high gravity gradient that reflects the fault F_1 (Figs. 2, 4). Previous studies indicate that the large-scale strike–slip movement of Tanlu fault (F_1) mainly took place during the Mesozoic and Paleogene and formed many tenso-shear and compresso-shear en-echelon faults (Meng et al. 2007). Thus, the en-echelon faults are closely related to the left-lateral and right-lateral strike–slip movements of the fault F_1 and were the result of the tenso-shear tectonic stress field generated by the left-lateral and right-lateral strike–slip movement.

Delineation of local structures

Local structures in this study refer to positive structures such as buried hills, anticlines, nose-shaped structures, and small faulted blocks, which are related to oil and gas reservoirs in the area. There are many methods to extract local anomalies from potential field data (Zeng, 2005); we used the vertical derivative of the residual anomalies.

Figure 13 shows the first vertical derivative of the residual gravity anomalies, which are shown in Fig. 4, together with known oil and gas reservoirs. The figure indicates that all of the oil and gas fields basically correspond to local gravity highs in the low gravity background or the nose-shaped anomalies at the edge of the low gravity background. Figure 14 shows a seismic profile, which displays

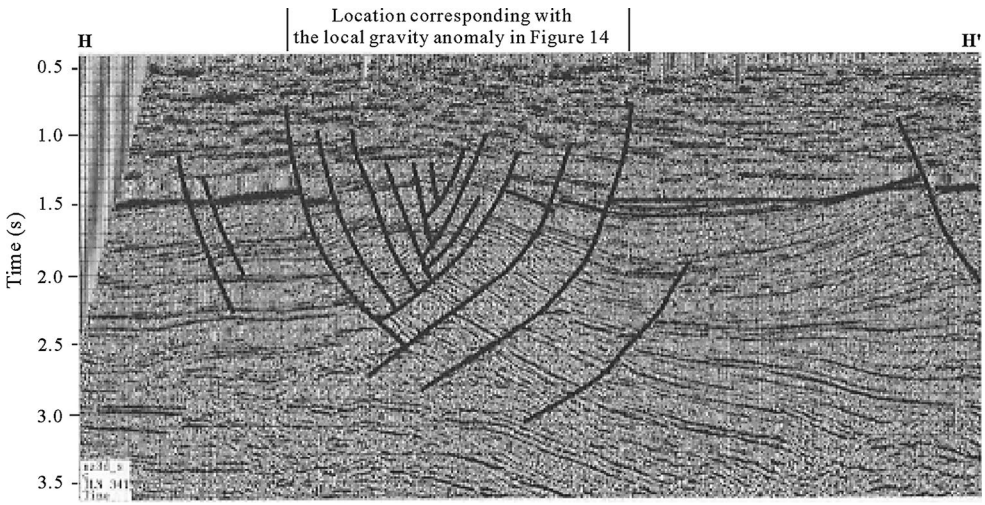

Fig. 14 Seismic profile showing the known oil field in Dongying sag (Fig. 7) of the study area (after Zhou et al. 2003). The location of this profile is shown in Fig. 13

an anticline corresponding to the local gravity high in Fig. 13. The exploration work showed that there are rich oil and gas resources accumulated during the Paleogene in local positive structures (e.g., anticlines, buried hills, nose-shaped structures and small faulted blocks). So, there are usually clear gravity responses (local gravity highs) for the positive local structures of a certain scale in the study area, and we can identify positive local structures using the vertical derivative of the residual anomalies.

We delineated the local structures by the following principles: (1) local gravity highs; (2) located in sags; and (3) the Cenozoic strata thicker in the sags. By a comprehensive analysis along with gravity inversion, we identified dozens of local structures. We classified them into 10 local structure belts (numbered sequentially in Fig. 13) according to their locations and relevance to the structural elements. Each belt consists of a few interrelated local structures. These belts should be favorable for hydrocarbon accumulation and could constitute more accurate targets for oil and gas exploration, including seismic imaging and drilling, in the future.

Conclusions

High-precision airborne gravity surveys, as a special geophysical method, can be carried out in complicated geographic conditions such as onshore–offshore transitional zones. Airborne gravity surveys are an effective supplement for regional geological surveys and mineral resource exploration in areas mapped poorly by conventional methods.

With airborne gravity data, sedimentary basins can be studied and analyzed with regard to the fault system, structural elements and styles, sedimentary thickness and local structures (belts). Gravity anomaly separation is the important foundation for basin analysis using airborne gravity data. We performed gravity anomaly separation using the wavelet transform method, and accurate results were obtained.

Based on the airborne gravity data collected over the central area of Bohai Bay Basin, we interpreted nearly 50 faults, divided the structural elements, calculated the depth to the Cenozoic basement, identified the structural styles and described the local structure belts. Among these, seven new faults and one new sag were discovered, and ten new local structure belts are delineated by the present airborne gravity.

Acknowledgments We thank the reviewers Ingo Heyde and Thomas Jahr and the Editor in Chief Prof. Wolf-Christian Dullo for their constructive and useful comments that have improved this paper. Special thanks are expressed to Professor Zhihong Guo of China Aero Geophysical Survey and Remote Sensing Center for Land and Resources, for his scientific contribution in data processing. Our sincere thanks also go to other technical personnel for their participation in data acquisition. This study was supported by the National Important Special Project of Science and Technology of China (Grant No.GZH201200301).

References

Aguilar-Rodriguez E, Rodriguez-Martinez M, Romero-Hernandez E, Mejia-Ambriz JC, Gonzalez-Esparza JA, Tokumaru M (2014) The wavelet transform function to analyze interplanetary scintillation observations. Geophys Res Lett 41:3331–3335

Ball P, Eagles G, Ebinger C, McClay K, Totterdell J (2013) The spatial and temporal evolution of strain during the separation of Australia and Antarctica. Geochem Geophys Geosyst 14:2771–2799

Beiki M (2013) TSVD analysis of Euler deconvolution to improve estimating magnetic source parameters: an example from the Asele area, Sweden. J Appl Geophys 90:82–91

Choi SC, Oh CW, Götze HJ (2013) Three-dimensional density modeling of the EGM2008 gravity field over the Mount Paekdu volcanic area. J Geophys Res Solid Earth 118:3820–3836

Diehl TM, Holt JW, Blankenship DD, Young DA (2008) First airborne gravity results over the Thwaites Glacier catchment, West Antarctica. Geochem Geophys Geosyst 9:1241–1450

Dransfield M, Zeng Y (2009) Airborne gravity gradiometry: terrain corrections and elevation error. Geophysics 74:137–142

Fedi M (2007) DEXP: a fast method to determine the depth and the structural index of potential fields sources. Geophysics 72:1–11

Fedi M, Cascone L (2011) Composite continuous wavelet transform of potential fields with different choices of analyzing wavelets. J Geophys Res Solid Earth 116:B7

Fedi M, Florio G (2013) Determination of the maximum-depth to potential field sources by a maximum structural index method. J Appl Geophys 88:154–160

Forsberg R, Olesen AV (2010) Airborne gravity field determination. In: Xu GC (ed) Sciences of Geodesy–I. Springer, Berlin, Heidelberg, pp 83–104

Forsberg R, Olesen AV, Einarsson I, Manandhar N, Shreshta K (2014) Geoid of Nepal from airborne gravity survey. Int Assoc Geodesy Symp 139:521–527

Goyal P, Tiwari VM (2014) Application of the continuous wavelet transform of gravity and magnetic data to estimate sub-basalt sediment thickness. Geophys Prospect 62:148–157

Gutierrez RR, Abad JD, Parsons DR, Best JL (2013) Discrimination of bed form scales using robust spline filters and wavelet transforms: methods and application to synthetic signals and bed forms of the Río Paraná, Argentina. J Geophys Res Earth Surf 118:1400–1418

Harlan WS (2014) Wavelet balancing for residual moveouts. Geophysics 79:V217–225

Kass MA (2013) Consequences of flight height and line spacing on airborne (helicopter) gravity gradient resolution in the Great Sand Dunes National Park and Preserve, Colorado. Lead Edge 32:932–938

Keating P, Pilkington M (2013) Analysis and reprocessing of airborne gravity gradiometer data over the Strange Lake rare Earth deposit, Quebec-Labrador. Lead Edge 32:940–947

Khalil MA, Santos FM, Farzamian M (2014) 3D gravity inversion and Euler deconvolution to delineate the hydro-tectonic regime in El-Arish area, northern Sinai Peninsula. J Appl Geophys 103:104–113

Kunagu P, Balasis G, Lesur V, Chandrasekhar E, Papadimitriou C (2013) Wavelet characterization of external magnetic sources as observed by CHAMP satellite: evidence for unmodelled signals in geomagnetic field models. Geophys J Int 192:946–950

Lee M, Morris W, Leblanc G, Harris G (2013) Curvature analysis to differentiate magnetic sources for geologic mapping. Geophys Prospect 61:572–585

Li WY, Zhou JX, Zhou XH, Guo ZH, An ZF, Xu JC, Li B, Luo F (2010a) Geological-genetic classification and prospecting significance on local anomaly of airborne gravimetry. Adv Earth Sci 25:1061–1069

Li WY, Zhou JX, Xiong SQ, Guo ZH, Xu JC, Zhou XH, An ZF, Li B, Luo F (2010b) Tectonic geometry of Tan-lu faults in the Bohai

Sea and its adjacent areas viewed from airborne gravity. Acta Geosci Sin 31:549–556

Li WY, Lu WF, Liu YX, Xu JC (2012) Superimposed versus residual basin: the North Yellow Sea basin. Geosci Front 3:33–39

Li WY, Zhou JX, Xiong SQ, Liu YX, Xu JC (2013) Study of residual basin and tectonolayering based on airborne gravity and magnetic data. Acta Geol Sin 87:1137–1153

Li WY, Liu YX, Xu JC (2014) Onshore–offshore structure and hydrocarbon potential of the South Yellow Sea. J Asian Earth Sci 90:127–136

Lucke OH (2014) Moho structure of Central America based on three-dimensional lithospheric density modelling of satellite-derived gravity data. Int J Earth Sci 103:1733–1745

Martin R, Monteiller V, Komatitsch D, Perrouty S, Jessell M, Bonvalot S, Lindsay M (2013) Gravity inversion using wavelet-based compression on parallel hybrid CPU/GPU systems: application to southwest Ghana. Geophys J Int 195:1594–1619

McAdoo DC, Farrell SL, Laxon S, Ridout A, Zwally HJ, Yi DH (2013) Gravity of the Arctic Ocean from satellite data with validations using airborne gravimetry: oceanographic implications. J Geophys Res Oceans 118:917–930

Meng QR, Li SY, Li RW (2007) Mesozoic evolution of the Hefei basin in eastern China: sedimentary response to deformations in the adjacent Dabieshan and along the Tanlu fault. Geol Soc Am Bull 119:897–916

Oruc B (2014) Structural interpretation of southern part of western Anatolian using analytic signal of the second order gravity gradients and discrete wavelet transform analysis. J Appl Geophys 103:82–98

Pacino MC, Jäger E, Forsberg R, Olesen A, Miranda S, Lenzano L (2014) Geoid model and altitude at Mount Aconcagua Region (Argentina) from Airborne Gravity Survey. Int Assoc Geod Symp 141:179–185

Salem A (2011) Multi-deconvolution analysis of potential field data. J Appl Geophys 74:151–156

Schwabe J, Scheinert M, Dietrich R, Ferraccioli F, Jordan T (2012) Regional geoid improvement over the Antarctic Peninsula utilizing airborne gravity data. Int Assoc Geod Symp 136:457–464

Speranza F, Minelli L (2014) Ultra-thick Triassic dolomites control the rupture behavior of the central Apennine seismicity: evidence from magnetic modeling of the L'Aquila fault zone. J Geophys Res Solid Earth 119:6756–6770

Su JB, Zhu WB, Wei J, Xu LM, Yang YF, Wang ZQ, Zhang ZY (2011) Fault growth and linkage: implications for tectonosedimentary evolution in the Chezhen Basin of Bohai Bay, eastern China. AAPG Bull 95:1–26

Tedla GE, Meijde M, Nyblade AA, Meer FD (2011) A crustal thickness map of Africa derived from a global gravity field model using Euler deconvolution. Geophys J Int 187:1–9

Vandas MI, Romashets EP (2014) Euler potentials for two current sheets of nonzero thickness along ambient uniform magnetic field. J Geophys Res Space Phys 119:2579–2592

Yuan YO, Simons FJ (2014) Multiscale adjoint waveform-difference tomography using wavelets. Geophysics 79:WA79–WA95

Zeng HL (2005) Gravity field and gravity exploration. Geological Publishing House, Beijing, pp. 63–65, 235–257

Zhou LH, Li SZ, Liu JZ (2003) Pre-Tertiary tectonic evolution and buried hill-type oil–gas development and reservation under the Bohai Bay basin. China Science and Technology Press, Beijing, pp 2–22